Transonic Navier-Stokes Solutions About a Generic Hypersonic Configuration

Farhad Ghaffari,* James M. Luckring,† and James L. Thomas‡
NASA Langley Research Center, Hampton, Virginia 23665
and
Brent L. Bates§
Vigyan, Inc., Hampton, Virginia 23666

Three-dimensional transonic viscous flow computations are presented for a generic high-speed accelerator model that includes wing, body, fillets, and a no-flow-through engine nacelle. Solutions are obtained from an algorithm for the compressible Navier-Stokes equations that incorporates an upwind-biased, flux-vector-splitting approach along with longitudinally patched grids. Results are presented for fully turbulent flow assumptions and include correlations with wind-tunnel data. A good quantitative agreement for the forebody surface pressure distribution is achieved between computations and the available wind-tunnel measurements at $M_\infty = 0.9$. Furthermore, it is demonstrated that the flow is stagnating around the boattail region due to separation from the aft-engine cowl lip.

Nomenclature

C_L = lift coefficient, lift/$q_\infty S_{\text{ref}}$
C_p = pressure coefficient, $(p - p_\infty)/q_\infty$
C_p^* = critical pressure coefficient
c_p = specific heat at constant pressure
c_v = specific heat at constant volume
E_0 = total energy per unit volume
$\hat{F},\hat{G},\hat{H}$ = flux vectors
h_0 = total enthalpy, $(E_0 + p)/\rho$
J = Jacobian of the coordinate transformation
k = conductivity, $c_p\mu/Pr$
l = total body length
M_∞ = freestream Mach number
Pr = Prandtl number
$\hat{Q}$ = state vector, $J^{-1}[\rho,\rho u,\rho v,\rho w,E_0]^T$
q = total velocity
q_∞ = freestream dynamic pressure
R_l = Reynolds number based on l
S_{ref} = area of reference wing planform
u,v,w = body-axis Cartesian velocity components
v^* = wall-friction velocity, $\sqrt{\tau_w/\rho}$
x/l = normalized longitudinal distance aft of nose
y^+ = inner-law variable, yv^*/v
α = angle of attack, deg
β,δ = residual parameters
γ = ratio of specific heats, c_p/c_v
μ = viscosity
ν = kinematic viscosity, μ/ρ
θ = azimuthal angle
ξ,η,ζ = body-fitted coordinates
ρ = density
τ_w = wall shear stress

Introduction

THE proposed National Aero-Space Plane (NASP) has revived interest in hypersonic flow research in the past few years, particularly in the area of computer algorithm developments. The design of such a vehicle inevitably would rely heavily on computational fluid dynamics (CFD), since the current ground test facilities are limited to lower speed regimes. Also, CFD results generally provide much more information about the flow structures and their detail mechanism than one can obtain experimentally.

The challenges associated with grid generation and surface definition, along with relatively large computational memory requirements, hamper the applications of advanced CFD-code methodologies to complex aircraft configurations. Nonetheless, recent progress has been shown for several cases, including subsonic inviscid flow computations about the complete F-14 configuration,[1] as well as transonic viscous flow about the F-16A.[2] In addition, viscous flow computations about the ascent configuration of the Space Shuttle[3] have shown good agreement with flight data at subsonic, transonic, and supersonic speeds. Most recently, three-dimensional viscous flow computations about the F/A-18 forebody-LEX configuration[4] have demonstrated good correlation with experimental wind-tunnel data, as well as with flight test results. Prior computations for generic NASP-type configurations have demonstrated the applicability of Navier-Stokes methodology to transonic[5] as well as hypersonic[6] flow, with Mach numbers exceeding 20.

The present investigation is directed toward applying an extended version of an implicit Navier-Stokes algorithm[7-10] to a generic hypersonic accelerator configuration at $M_\infty = 0.9$, $R_l \approx 30 \times 10^6$, and $\alpha = 2$ deg. At these conditions, the flow is assumed to be fully turbulent, hence only turbulent computations are performed. The algorithm permits longitudinally blocked grids, which is an efficient procedure for accurately modeling the subject configuration. The accelerator geometry has been selected for this study primarily due to the availability of current transonic wind-tunnel data,[11,12] as well as a growing interest at NASA in utilizing the state-of-the-art CFD codes to analyze the flow about the NASP-type configuration in all speed regimes.

Presented as Paper 90-0430 at the AIAA 28th Aerospace Sciences Meeting, Reno, NV, Jan. 8–11, 1990; received March 21, 1990; revision received July 6, 1990; accepted for publication July 8, 1990.

*Research Engineer, Transonic Aerodynamics Branch, Applied Aerodynamics Division. Senior Member AIAA.
†Assistant Branch Head, Transonic Aerodynamics Branch, Applied Aerodynamics Division. Associate Fellow AIAA.
‡Senior Research Scientist, Computational Methods Branch, Fluid Mechanics Division. Associate Fellow AIAA.
§Research Engineer. Member AIAA.

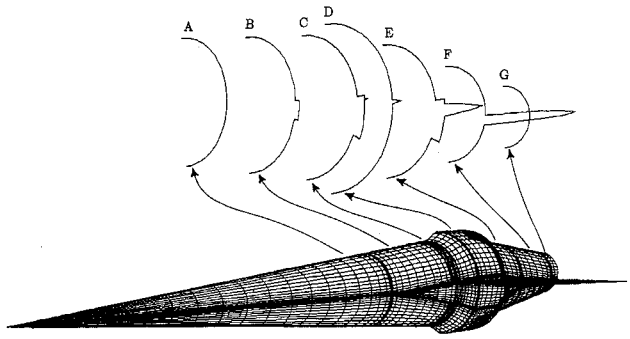

Fig. 1 Accelerator surface and cross-sectional grid.

Governing Equations

The governing equations as well as computational method for the present investigation have been published many times in the open literature[7-10] as they have evolved. The flow is presumed to be governed by the unsteady Reynolds-averaged Navier-Stokes equations, which are written in a body-fitted coordinate system. They are written in a usual conservation-law form as

$$\hat{Q}_{,t} + (\hat{F} - \hat{F}_v)_{,\xi} + (\hat{G} - \hat{G}_v)_{,\eta} + (\hat{H} - \hat{H}_v)_{,\zeta} = 0 \qquad (1)$$

Here the subscripts with a comma denote partial differentiation, the subscript v identifies the viscous terms, and the superscript $\hat{}$ indicates scaling with respect to the Jacobian of the coordinate transformation. With the ideal gas assumption, the pressure and the total enthalpy can be expressed as

$$p = (\gamma - 1)\left(E_0 - \frac{1}{2}\rho q^2\right) \qquad h_0 = \frac{\gamma}{\gamma - 1}\frac{p}{\rho} + \frac{1}{2}q^2 \qquad (2)$$

For the present study, the thin layer approximation to the governing equations is invoked (i.e., $\hat{F}_v = \hat{G}_v = 0$), thus accounting for viscous flux terms only in the ζ direction (normal to the body).

Turbulence effects are accounted for through the notion of an eddy viscosity and eddy conductivity:

$$\mu = \mu_l + \mu_t = \mu_l(1 + \mu_t/\mu_l) \qquad (3)$$

$$k = k_l + k_t = k_l(1 + k_t/k_l)$$

$$= (c_p\mu_l)/(Pr_l)[1 + (\mu_t Pr_l)/(\mu_l Pr_t)) \qquad (4)$$

Here the subscripts l and t denote laminar and turbulent, respectively. The algebraic turbulence model developed by Baldwin and Lomax[13] is used to evaluate appropriate turbulence quantities. For separated flow regions, the notions of Degani and Schiff[14] are drawn upon to determine proper turbulence length scales.

Computational Method

Discretization of the governing equations results in a consistent approximation to the conservation laws in integral form:

$$\frac{\partial}{\partial t}\int\int\int \hat{Q}\, dV + \int\int \hat{f}\cdot\hat{n}\, dS = 0 \qquad (5)$$

where the rate of change of the state vector $\hat{Q}$ within a cell is balanced by the net flux $\hat{f}$ across the cell surface. The convective and the pressure terms arising in the flux quantities are represented using an upwind-biased algorithm, with either the flux-vector-splitting approach of van Leer[15] or the flux-difference-splitting approach of Roe.[16] Both approaches rely on a reconstruction of primitive variable data at the cell centers to the cell interfaces; the reconstruction is limited in such a way to reduce oscillations near discontinuities, such as shocks, and is third-order accurate in the special case of one-dimensional flows. The shear stress and the heat transfer terms are centrally differenced so that the resulting algorithm is spatially second-order accurate. Solutions are advanced in time with a spatially split approximate factorization method that, in general, solves a series of block 5×5 tridiagonal matrices to advance the solution to a new time level. For the flux-difference-splitting scheme, the implicit terms are diagonalized, leading to a series of scalar tridiagonal inversions.

In the present computations, attempts were made initially to use flux-difference splitting with third-order accuracy. However, due to convergence difficulties, the alternative flux-vector-splitting approach was invoked. Prior results[17] have shown the van Leer scheme to diffuse boundary layers, particularly when utilized with first-order accuracy and/or with sparse grid resolution. This limitation was overcome in the present work by utilizing the van Leer scheme with third-order accuracy and by performing the computations with a sufficiently dense mesh.

Information is exchanged between the longitudinal blocks using the patching algorithm described by Thomas et al.[10] At the interface between the two blocks, the dependent variables at the cell centers of each zone are interpolated across the coincident interface boundary assuming a biquadratic variation across each cell of the opposing zone. The interpolation is second-order accurate and conserves the mass, momentum, and energy across the zonal interface only to within the truncation error of the discrete solution.

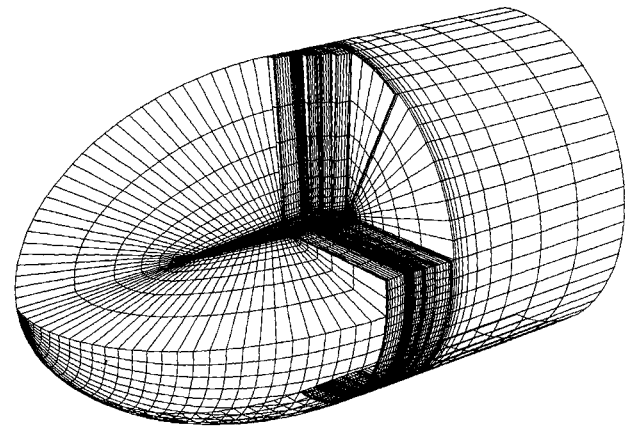

Fig. 2a Blocking strategy for the accelerator configuration—far-field view.

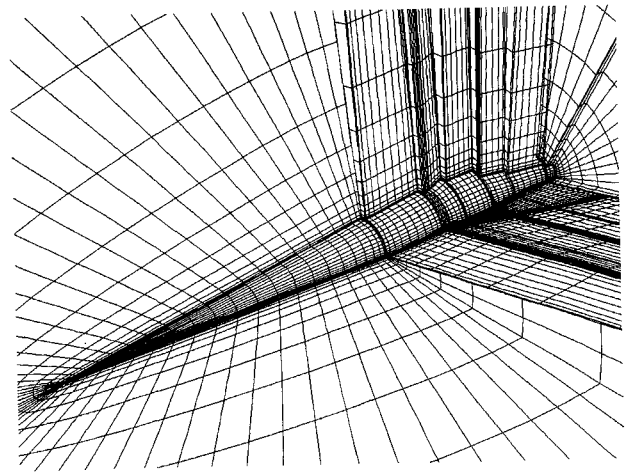

Fig. 2b Blocking strategy for the accelerator configuration—near-field view.

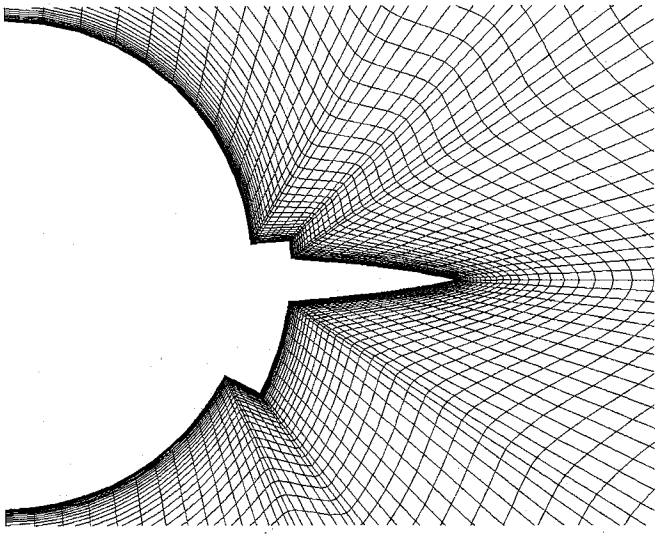

Fig. 3 A typical accelerator crossflow grid.

Experimental Models

There were two accelerator models tested in the Langley 16-ft transonic wind tunnel. The first model was a sting-mounted model with an open inlet and exhaust faces (i.e., flow-through). This model, called the "forebody" model, was intended to only provide experimental pressure data on the forebody. The second model, called the "propulsion" model, had a faired over (closed) inlet and open exhaust face to allow for the simulation of propulsion effects. This model was mounted on a strut that housed some of the exhaust jet-flow propulsion apparatus. The experiment was designed to obtain experimental pressure measurements on the boattail region for various exit mass fluxes including zero (i.e., a jet-off case).

Numerical Model Representation

The surface grid definition is obtained from an analytical representation of the configuration. The complete surface representation of the configuration along with various longitudinal cuts are shown in Fig. 1. The body of the configuration consists of a 5-deg half-angle right-circular cone and a 9-deg boattail frustum that are connected with a cylinder. A nacelle is wrapped around the cylindrical part of the body. The configuration incorporates wing fillets in front and behind the engine cowl. The front-engine wing fillet blends into the nacelle cowl at a longitudinal station between stations C and D (Fig. 1). The aft-engine wing fillet merges smoothly into the wing upper and lower surfaces, at a longitudinal station between stations E and F. The configuration included a 70-deg swept sharp delta wing with a span of $0.11 \times l$. The wing had a 4% thick biconvex airfoil and was mounted at 3-deg incidence on the combination of front- and aft-engine fillets as well as the nacelle.

The inlet face is faired over similar to the tested wind-tunnel propulsion model. Since the effects of propulsion are not included in the present computations, the exhaust face was also faired over with a 45-deg ramp. This fairing eliminates the problem of having a surface discontinuity at the exit plane, where there needs to be a longitudinal patching station of two blocks from a geometrical consideration (i.e., start of the aft fillet). The surface geometry is defined with a total of 5400 grid points at 88 longitudinal stations along the body.

The field grid is divided into eight longitudinal blocks, each representing a local geometrical complexity of the configuration. The forebody block is generated with a C-O grid topology, thus resolving the nose radius and extending to the upstream inflow boundary. The three-dimensional grid for the remaining blocks is constructed from two-dimensional O-type crossflow grids that are longitudinally stacked, constituting an H-O topology. Figure 2 illustrates a far-field as well as a near-field view of complete grid about the accelerator configuration. The grid lines in the radial direction are plotted for every fourth point for clarity. The grid dimensions as well as the mesh topology for each corresponding block are listed in Table 1.

Table 1 Grid dimensions and topology

Block	x	θ	r	Points	Top
1	29	31	65	58,435	C-O
2	12	59	65	46,020	H-O
3	12	91	65	70,980	H-O
4	9	79	65	46,215	H-O
5	13	91	65	76,895	H-O
6	9	75	65	43,875	H-O
7	4	31	65	8060	H-O
8	11	31	65	22,165	H-O

The upstream, downstream, and the radial extent of the flowfield grid is about one configuration body length, which corresponds to 13.5 times the maximum body diameter. Block 8 is the downstream extension of the grid and has 11 longitudinal stations. All blocks have 65 points in the radial direction, and the circumferential number of grid points varies from block to block, depending on the complexity of the local cross-sectional geometry. Longitudinally, the grids are clustered near each geometrical break, such as a station where the wing starts or terminates. There are approximately 373,000 grid points used to represent the entire flowfield domain.

The crossflow grids are generated using established transfinite interpolation techniques[18,19] with a method applicable to slender shapes.[4,6] The flowfield grid is generated with sufficient normal clustering near the surface to adequately resolve the laminar sublayer of the turbulent boundary-layer flow at the subject wind-tunnel freestream conditions ($M_\infty = 0.9$, $R_l \approx 30 \times 10^6$, $\alpha = 2$ deg). This grid produced an average normal cell-center size next to the wall of approximately $10^{-5}l$, which corresponded to $y^+ \approx 3$ for the turbulent computations; a laminar sublayer generally extends to $y^+ \approx 8.5$. The adequacy of the grid clustering was further assessed by examining the velocity profiles at various locations along the body. The solutions revealed that, for example, at about mid-forebody length, there were approximately 17 points within the first 90% of the boundary layer, with 2–3 points in the laminar sublayer. Figure 3 illustrates the near-field view of a typical configuration cross section, as well as the grid resolution in the vicinity of the fillet-body and fillet-wing juncture. This figure illustrates the challenge that is associated with generating a single O-type grid around such a complex cross section, with various break points in the surface geometry.

Results and Discussion

Results are presented first for general flow features. This is followed by a comparison between the computed surface pressures and experimental data on the forebody as well as boattail region. Finally, a discussion on the convergence attributes of the computed results is presented.

Solution Attributes

Mach contours slightly off the surface (i.e., second grid point in the normal direction) and in the configuration plane of symmetry at the subject wind-tunnel flow conditions are shown in Fig. 4. The Mach contours range from ≈ 0.0 (near the surface) to 1.60 (near the engine cowl lip) with an increment of 0.08. In addition, the sonic line is displayed to highlight the supersonic flow region. This figure indicates that after a basically subsonic forebody, the flow accelerates supersonically over the faired over inlet, followed by a mild compression on the engine cowl; it subsequently shocks down at

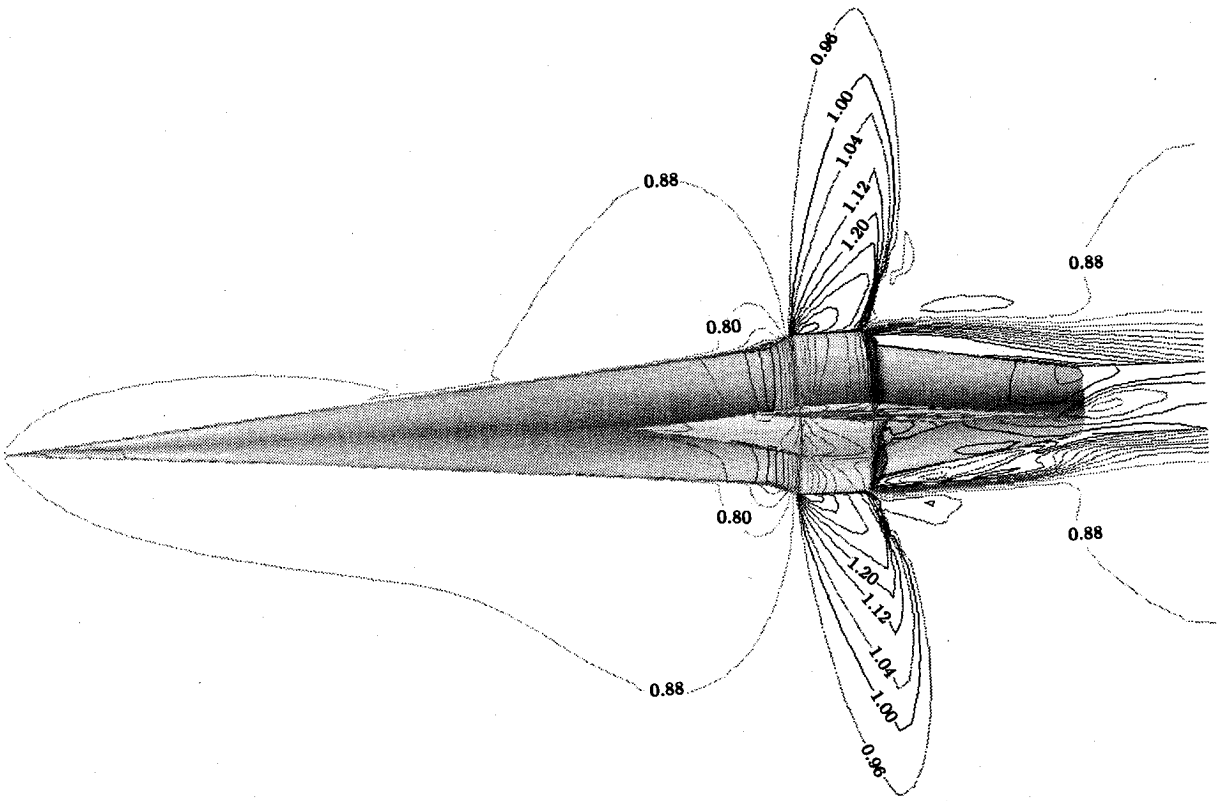

Fig. 4 Surface and plane of symmetry Mach contours: $M_\infty = 0.9$, $R_l \approx 30 \times 10^6$, $\alpha = 2$ deg.

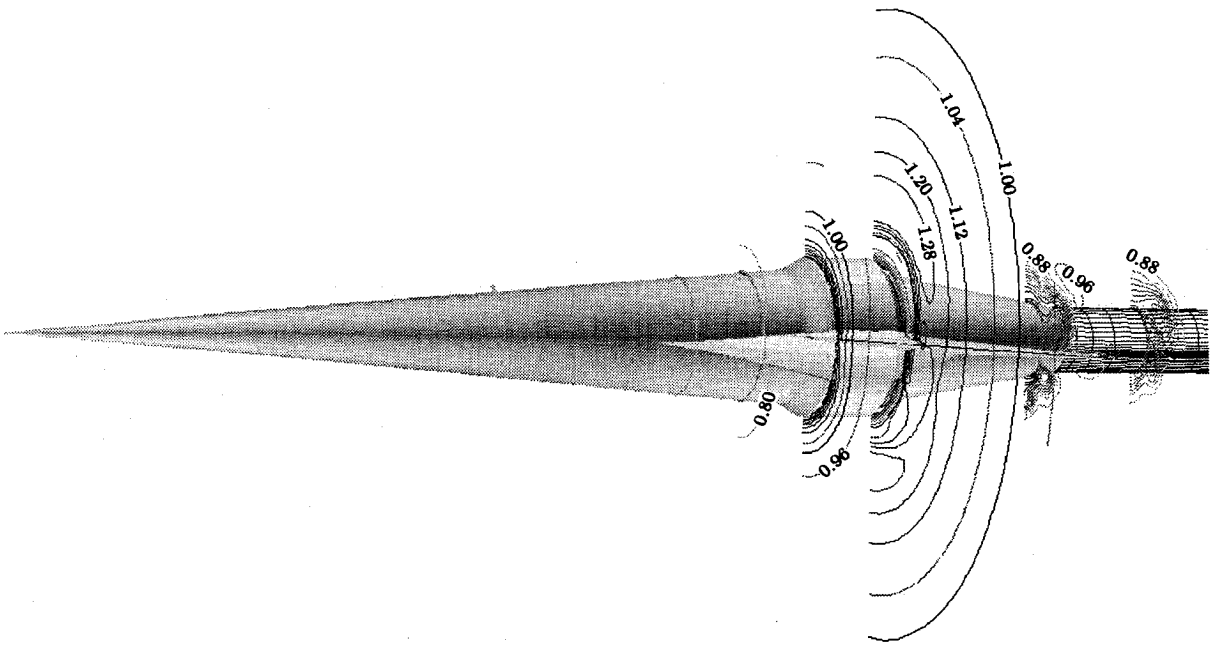

Fig. 5 Mach contours in crossflow plane: $M_\infty = 0.9$, $R_l \approx 30 \times 10^6$, $\alpha = 2$ deg.

the aft-engine cowl lip. The presence of the shock along with the slanted exhaust face produces an adverse pressure gradient that causes the flow to separate at the exhaust cowl lip, enveloping the entire boattail region. Note that the Mach contours smoothly cross over the many block interfaces. Crossflow Mach contours are shown in Fig. 5 for various planes along the length of the configuration. This figure illustrates the radial extent of the supersonic zone in two crossflow planes: one on the nacelle and the other slightly aft of it cutting through the shock. In addition, the complex flow structure in the separated boattail region is well depicted in the last two crossflow planes. It is speculated that propulsion effects (e.g., either a simple flow-through case or an actual engine simulation) should have a significant influence on the supersonic region as well as the separated flow in the boattail region.

The total pressure contours in various crossflow planes along the body as well as in the plane of symmetry are shown in Fig. 6a. The flow appears to be primarily attached on the forebody. Also, the losses that are associated with viscous flow are well illustrated in the separated boattail region. Figure 6b shows a closeup view of the total pressure contours

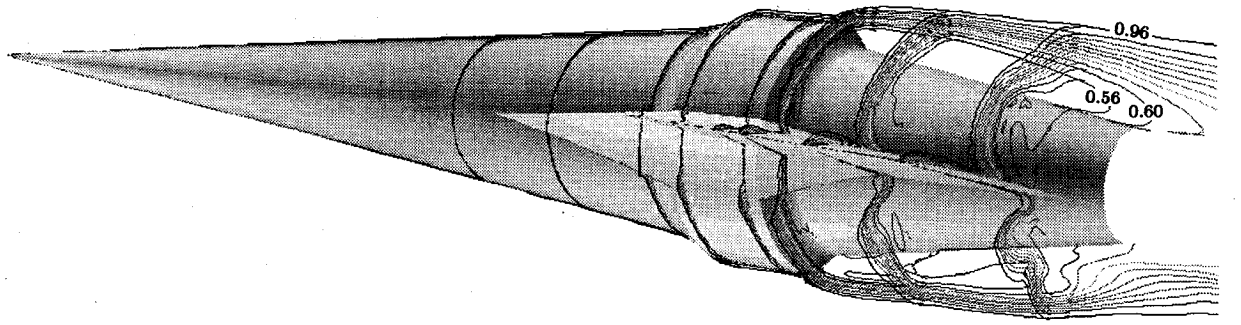

Fig. 6a Total pressure contours in crossflow and plane of symmetry—overall view: $M_\infty = 0.9$, $R_l \approx 30 \times 10^6$, $\alpha = 2$ deg.

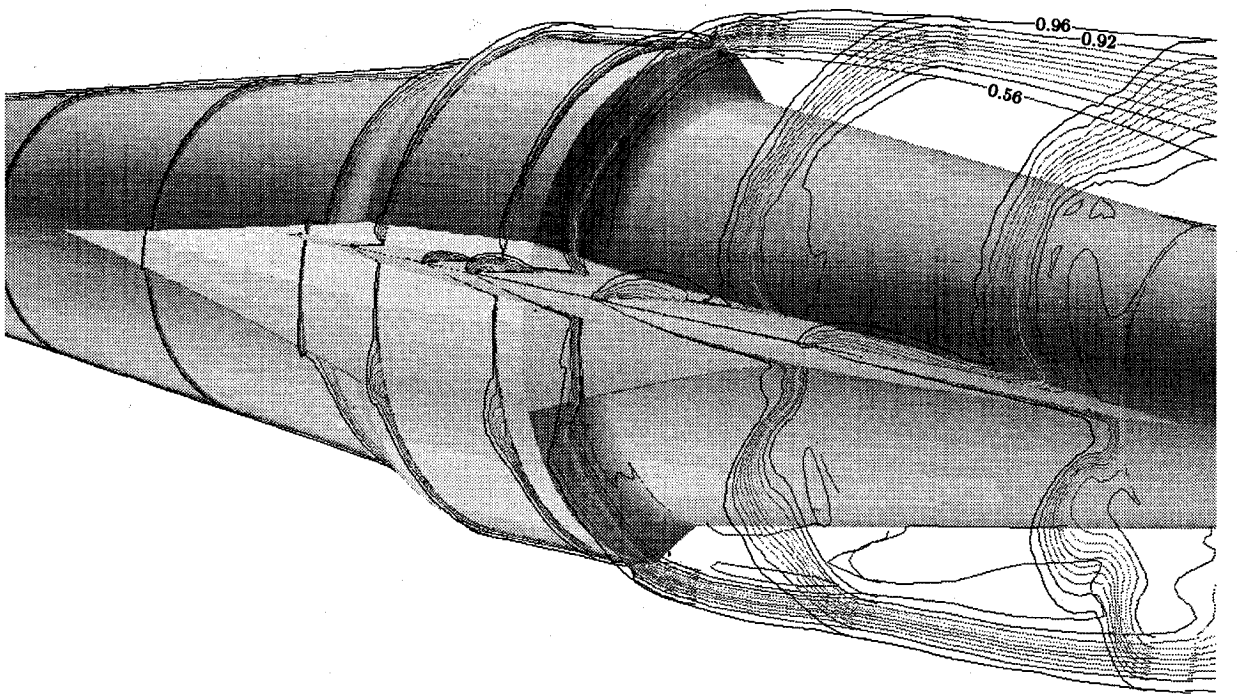

Fig. 6b Total pressure contours in crossflow and plane of symmetry—closeup view: $M_\infty = 0.9$, $R_l \approx 30 \times 10^6$, $\alpha = 2$ deg.

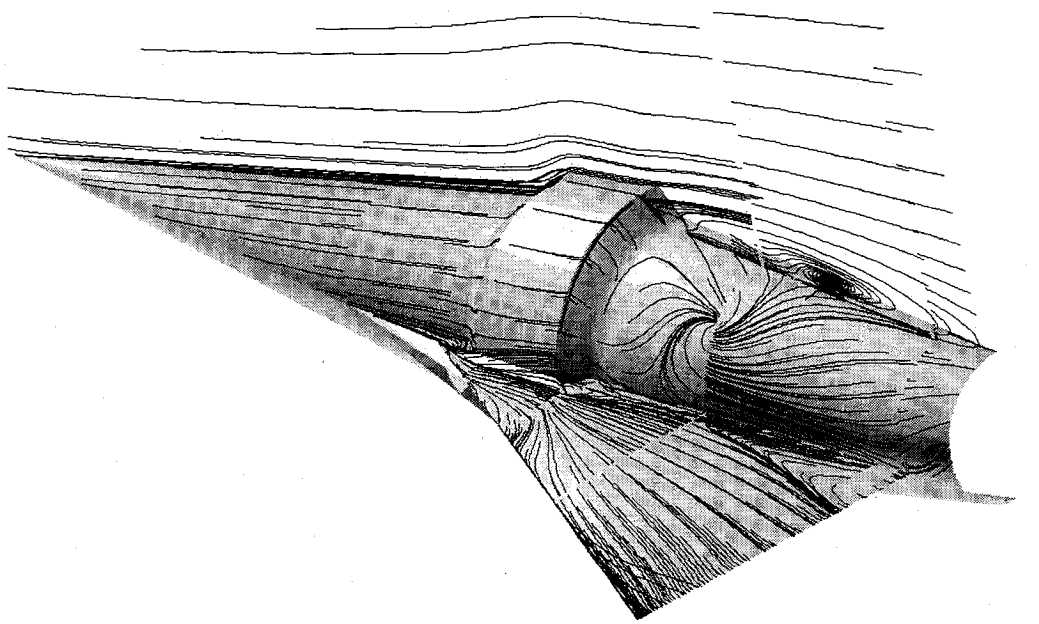

Fig. 7 Streamline pattern on the surface and plane of symmetry: $M_\infty = 0.9$, $R_l \approx 30 \times 10^6$, $\alpha = 2$ deg.

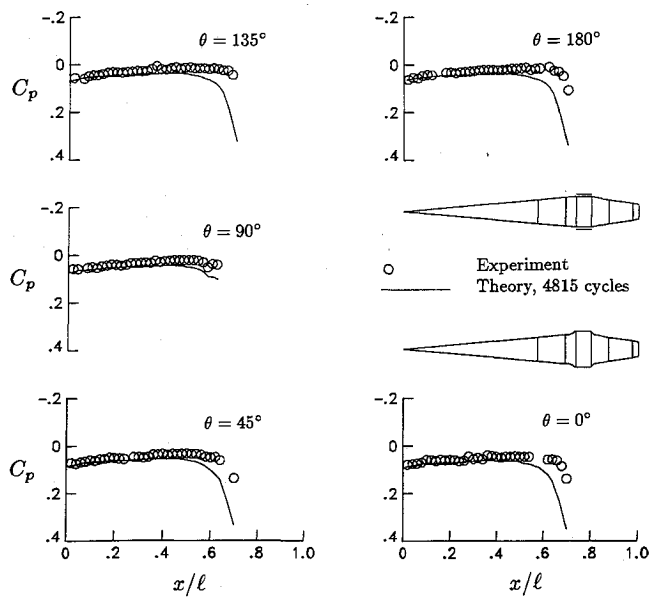

Fig. 8 Forebody surface pressure correlation with experiment: $M_\infty = 0.9$, $R_l \approx 30 \times 10^6$, $\alpha = 2$ deg.

to highlight the smaller separated flow structures that exist on the engine cowl as well as the wing upper surface. The separated flow on the cowl is associated with the fillet-body juncture flow that is spilling over the cowl on its lower surface and, to a lesser degree, on its upper surface. The small flow structure on the wing upper surface is evidence of a leading-edge bubble-type separation. The flow intensity at the center of this separated flow is reduced significantly as it passes through the shock that is located at the aft-engine cowl lip and extends over the wing surface.

The computed streamlines on the configuration upper surface as well as in the plane of symmetry are presented in Fig. 7. This figure clearly shows the abrupt change in the streamline pattern on the wing upper surface near the aft-engine cowl lip, due to the shock. The turning of the surface flow streamlines is primarily associated with the diminished axial velocity component of the flow. As a result, some of the affected streamlines on the upper surface appear to wrap around the leading edge and advance to the lower surface exhibiting an inboard trajectory near the wing tip. Figure 7 also shows the very complex surface flow pattern that is associated with the low-speed flow in the boattail region; this pattern appears to indicate a whorl.

Data Comparison

The computed static pressure coefficients on the forebody are compared with the experimentally measured data[11,12] in Fig. 8. The figure shows the comparison at five different conical rays from windward ($\theta = 0$ deg) to leeward side ($\theta = 180$ deg) in 45-deg increments. A schematic side view of the accelerator body for both the wind-tunnel and computational model is also shown to highlight the major geometrical differences that exist between them. As described previously the experimental forebody pressures were obtained on the same model, but only for flow through inlet conditions, whereas the numerical model had the faired over inlet and exhaust face. The longitudinal extent of the forebody covers approximately 70% of the configuration total body length. This figure reveals a good correlation between experimental data and the computed results up to $x/l \approx 0.4$. The discrepancies between theory and data in x/l range of 0.4–0.7 are mainly due to the differences in inlet flow conditions. The faired over inlet produces additional compression that results in more positive pressures, as indicated in the computed results of Fig. 8.

The computed pressure coefficients on the boattail are plotted against the measured data in the left half of Fig. 9, along the configuration plane of symmetry. This figure also shows a schematic side view of the experimental and computational model to illustrate the major differences that exist in the exhaust face with regard to the geometry and the flow condition. The data correspond to the experimental condition of zero-mass flux across the exit. This figure reveals a fairly good correlation between theory and experiment. The discrepancies in the neighborhood of the exit could well be due to geometrical differences at the exit face and/or the back pressure effects from the open exhaust face in the experiment.

The circumferential theoretical and the experimental data for two longitudinal stations on the boattail region are shown in the right half of Fig. 9. The first station is located slightly aft of the shock ($x/l = 0.828$) and the other further downstream ($x/l = 0.961$). Notice that the scales have been magnified to bring out the differences. At $x/l = 0.828$ there are some disagreements between theory and experiment, although the circumferential trend appears to have been better predicted. At $x/l = 0.961$ the agreement between theory and

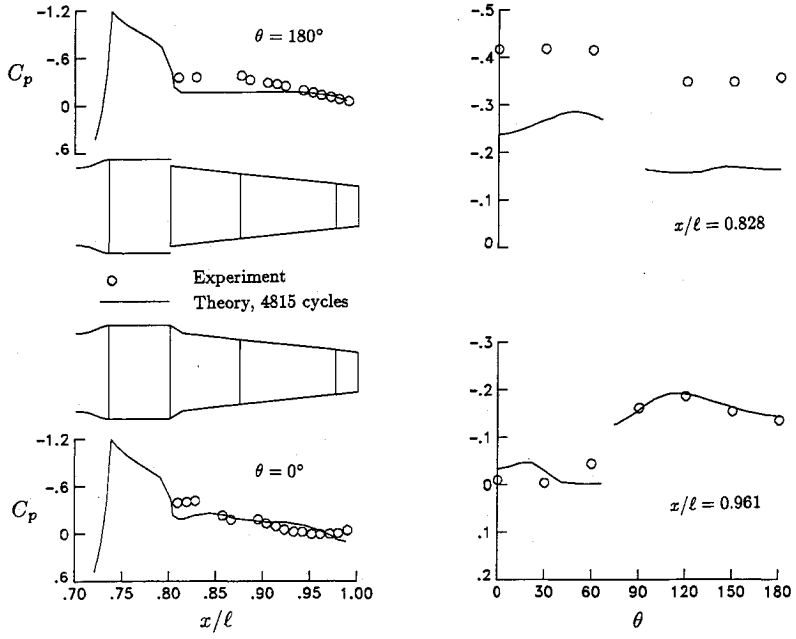

Fig. 9 Boattail surface pressure correlations with experiment: $M_\infty = 0.9$, $R_l \approx 30 \times 10^6$, $\alpha = 2$ deg.

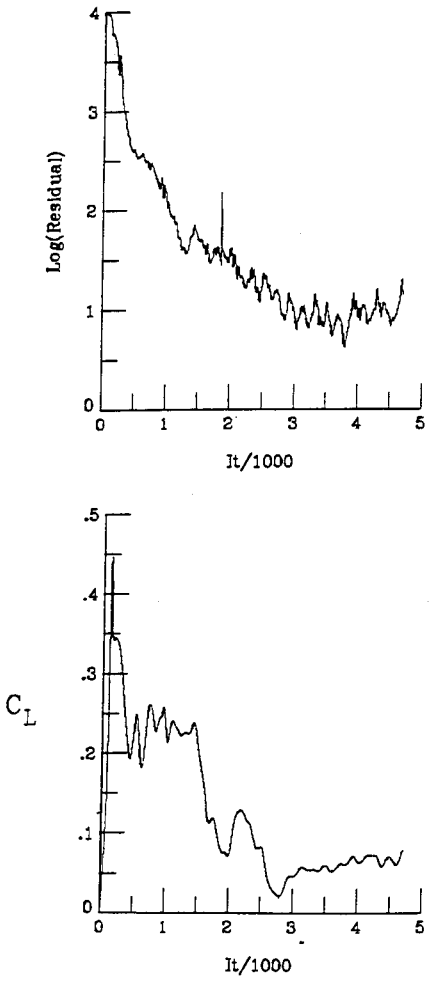

Fig. 10 Overall convergence history: $M_\infty = 0.9$, $R_l \approx 30 \times 10^6$, $\alpha = 2$ deg.

experiment is quite good. In general, the flow structure in the boattail region is very complex, and the correlations that have been achieved there are perhaps better than might have been expected.

Convergence Characteristics

The flow computations were performed on the NAS Cray 2, located at NASA Ames. On this machine, the algorithm requires approximately 50 μs per grid point per cycle. The present numerical results were obtained in nominally 4815 cycles, which required about 25 h of computer time. This number of cycles was sufficient to reduce the residuals by three orders of magnitude and limit the oscillations in C_L to $\approx \pm 0.005$ (Fig. 10). The computations were performed without the use of mesh sequencing or multigrid iteration.

The salient features of the flow were examined during the course of the convergence process. It was found that the position of the shock and the shape of the supersonic pocket were apparently established within approximately the first 2000 cycles. The loss in C_L, shown in Fig. 10, for 1500 $\leq$ iterations $\leq$ 2000 is primarily associated with the formation of separated flow in the boattail region. Subsequent to establishing the shock structure (iteration $\approx$ 2000), changes in this separated flow region result in a further loss of lift for the next $\approx$1000 cycles, after which changes in lift become small. The separated flow region appears to exhibit certain unsteady flow characteristics that are associated with the downstream convection of flow quantities from the exhaust face. There are reasons to believe that this separated region is the primary cause of the oscillations in the lift, as well as the residual magnitude for the last 1500 cycles (see Fig. 10).

To examine this conjecture, the individual block rms residuals (β_n) are appropriately weighted by the fraction of grid points in each block:

$$\delta_n^2 = \left[\frac{np_n}{np_{\text{total}}}\right](\beta_n)^2 \tag{6}$$

where

$$(\beta_n) = \sqrt{\frac{1}{np_n}\sum_{i=1}^{i=np_n} \text{residual}_i^2} \tag{7}$$

In the preceding equations, residual$_i$ refers to the residual in cell i and np_n refers to the number of points for block n. The total rms residual for the complete configuration can now be obtained from

$$\text{residual}_{\text{total}} = \sqrt{\sum_{n=1}^{N} \delta_n^2} \tag{8}$$

where N is the total number of blocks. The block residual distribution is presented in Fig. 11 for four different levels of iterations. This figure shows that the incremental local residual for blocks 5–7 are relatively more dominant than the corresponding residuals for the upstream blocks 1–4. The separation in the boattail region is mainly responsible for the large local residuals, as well as for their oscillatory behavior with the number of iterations. This separation also appears to be the principal cause for the excessive total number of iterations performed to achieve the present results. Note that the local block residual for the first four blocks are not changing much by advancing the solution from 2455 to 4815 cycles; the flow on the forebody appears to have set up within the first 2455 cycles.

The surface pressure sensitivity on the developing solution was also examined at three iteration levels. Figure 12 illustrates longitudinal pressure distributions on the accelerator configuration at two conical rays; $\theta = 0$ deg corresponds to the windward and $\theta = 180$ deg to the leeward side of the configuration plane of symmetry. The left half of Fig. 12 shows the surface pressures on the forebody along with a schematic side view of the computational accelerator body to highlight the longitudinal extent of the forebody. As discussed previously in the solution attributes, the forebody appears to exhibit a fairly benign flow condition, with the expected flow compression in the vicinity of the inlet face. It is also evident that the computed surface pressures are less sensitive to the last 1310 cycles beyond 3505.

The boattail surface pressure sensitivity in the plane of symmetry for the same number of cycles is shown in the right

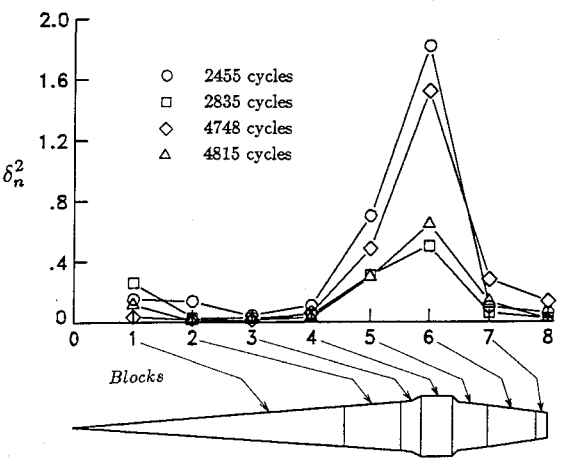

Fig. 11 Block residual history: $M_\infty = 0.9$, $R_l \approx 30 \times 10^6$, $\alpha = 2$ deg.

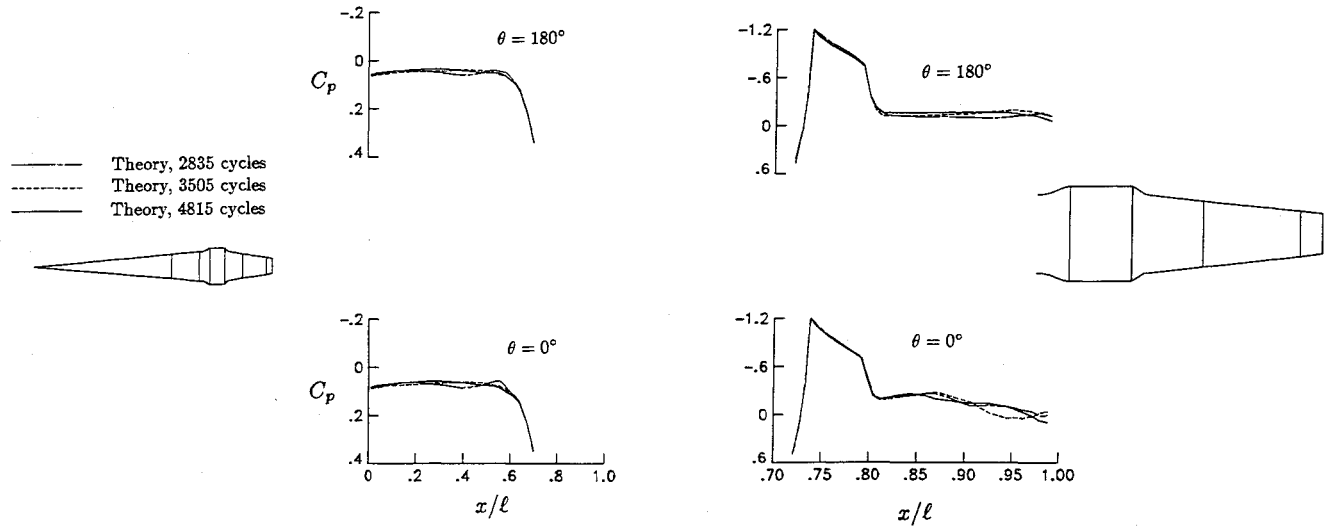

Fig. 12 Surface pressure sensitivity on solution development: $M_\infty = 0.9$, $R_l \approx 30 \times 10^6$, $\alpha = 2$ deg.

half of Fig. 12. This is basically the continuation of the forebody pressures onto the engine cowl and the boattail region. Note that these plots have scales that are different from those shown in the left half. The flow accelerates over the faired over inlet supersonically ($C_p^* \approx -0.2$) and then it goes through a mild compression over the engine cowl and subsequently shocks down at the aft-engine cowl lip. Note that the supersonic region, as well as the shock strength and its position, are well established with ≈2800 cycles. However, the pressures on the boattail region appear to be somewhat sensitive to those number of cycles examined.

In summary, the results from the surface pressure sensitivity study (for further discussion see Ref. 20) indicate that the flow on the forebody appears to have been well established within the first 3500 cycles. These results also reveal that the supersonic pocket over the engine cowl as well as the shock position and its strength were fully developed at about 2800 iterations. Furthermore, the flow in the separated boattail region was most sensitive to the number of cycles. Note that these results complement the findings discussed earlier from the residual-history point of view.

Concluding Remarks

Three-dimensional transonic viscous flow computations for a complex high-speed accelerator are presented with fully turbulent flow assumptions. The computed results show a large supersonic pocket over the nacelle surface with a shock at the aft-engine cowl lip. The presence of the shock as well as of the slanted exhaust face cause the flow to separate into a very complex flow structure enveloping the entire boattail region. This massive boattail separation appears to exhibit certain locally confined unsteady flow characteristics that do not significantly effect the flow outside of the separated zone. Reasonable qualitative comparisons are obtained between theoretical and experimental surface pressures in the separated boattail region. Furthermore, a good correlation between experimental static pressures and computational results on the forebody are disclosed.

Acknowledgments

NASA Langley Research Center sponsored the work of the fourth author under NASA Contract NAS1-18585.

References

[1]Szema, K. Y., Chakravarthy, S. R., and Bihari, B. L., "F-14 Flow Field Simulation," AIAA Paper 89-0642, Jan. 1989.

[2]Flores, J., and Chaderjian, N. M., "The Numerical Simulation of Transonic Separated Flow About the Complete F-16A," AIAA Paper 88-2506, June 1988.

[3]Buning, P. G., Chiu, I. T., Obayashi, S., Rizk, Y. M., and Steger, J. L., "Numerical Simulation of the Integrated Space Shuttle Vehicle in Ascent," AIAA Paper 88-4359, Aug. 1988.

[4]Ghaffari, F., Luckring, J. M., Thomas, J. L., and Bates, B. L., "Navier-Stokes Solutions about the F/A-18 Forebody-LEX Configuration," AIAA Paper 89-0338, Jan. 1989.

[5]Shrewsbery, G. D., Vadyak, J., Schuster, D. M., and Smith M. J., "Computation of Aircraft Component Flow Fields at Transonic Mach Numbers Using a Three-Dimensional Navier-Stokes Algorithm," NASA CP-3020, Vol. I, April 1988.

[6]Richardson, P. F., and Morrison, J. H., "Displacement Surface Calculations for a Hypersonic Aircraft," AIAA Paper 87-1190, June 1987.

[7]Thomas, J. L., and Newsome, R. W., "Navier-Stokes Computations of Lee-Side Flows Over Delta Wings," AIAA Paper 86-1049, May 1986.

[8]Thomas, J. L., Taylor, S. L., and Anderson, W. K., "Navier-Stokes Computations of Vortical Flows Over Low Aspect Ratio Wings," AIAA Paper 87-0207, Jan. 1987.

[9]Vatsa, V. N., Thomas, J. L., and Wedan, B. W., "Navier-Stokes Computations of Prolate Spheroids at Angle of Attack," AIAA Paper 87-2627, Aug. 1987.

[10]Thomas, J. L., Walters, R. W., Taekyu, R., Ghaffari, F., Weston, R. P., and Luckring, J. M., "A Patched Grid Algorithm for Complex Configurations Directed Towards the F-18 Aircraft," AIAA Paper 89-0121, Jan. 1989.

[11]Henderson, W. P., Lamb, M., and Bennet, B. D., "Aerodynamic Characteristics of a Powered Accelerator Model at Transonic Speeds (U)," Presented at the Fifth National Aero-Space Plane Technology Symposium, Monterery, CA, Paper 85, Oct. 1988.

[12]Henderson, W. P., and Bennet, B. D., "Forebody Pressure Distributions on a Conical Aerospace Plane Concept at Mach Numbers From 0.4 to 1.20 (U)," NASP TM-1078, Aug. 1989.

[13]Baldwin, B. S., and Lomax, H., "Thin Layer Approximation and Algebraic Model for Separated Turbulent Flows," AIAA Paper 78-257, Jan. 1978.

[14]Degani, D., and Schiff, L. B., "Computation of Supersonic Viscous Flows Around Pointed Bodies at Large Incidence," AIAA Paper 83-0034, Jan. 1983.

[15]Van Leer, B., "Flux-Vector Splitting for the Euler Equations," Institute for Computer Applications in Science and Engineering, ICASE Rept. 82-30, Sept. 1982.

[16]Roe, P. L., "Characteristic Based Schemes for the Euler Equations," *Annual Review of Fluid Mechanics*, Vol. 18, 1986, pp. 337–365.

[15]Van Leer, B., Thomas, J. L., Roe, P. L., and Newsome, R. W., "A Comparison of Numerical Flux Formulas for the Euler and Navier-Stokes Equations," AIAA Paper 87-1104, June 1987.

[18]Eriksson, L. E., "Practical Three-Dimensional Mesh Generation Using Transfinite Interpolation," *Journal of Fluid Mechanics*, Vol. 148, 1984, pp. 45–78.

[19]Smith, R. E., *Algebraic Grid Generation. Numerical Grid Generation,* Elsevier, New York, 1982, pp. 137–168.

[20]Ghaffari, F., Luckring, J. M., Thomas, J. L., Bates, B. L., "Transonic Navier-Stokes Solutions About a Complex High-Speed Accelerator Configuration," AIAA Paper 90-0430, Jan. 1990.